



RESEARCH ARTICLE

10.1029/2019JF005192

Decoupling the Role of Inertia, Friction, and Cohesion in Dense Granular Avalanche Pressure Build-up on Obstacles

M. L. Kyburz^{1,2} , Betty Sovilla¹ , Johan Gaume^{1,3} , and Christophe Ancey² 

¹WSL Institute for Snow and Avalanche Research SLF, Davos, Switzerland, ²Environmental Hydraulics Laboratory, Swiss Federal Institute of Technology, Lausanne, Switzerland, ³Snow and Avalanche Simulation Laboratory SLAB, Swiss Federal Institute of Technology, Lausanne, Switzerland

Key Points:

- We simulate impact pressure of cohesive granular flows on obstacles with the discrete element method
- The impact pressure on structures consists of the inertial, frictional, and cohesive contributions
- The strength of force chains and size of the mobilized domain govern the pressure buildup

Supporting Information:

- Supporting Information S1

Correspondence to:

M. L. Kyburz,
kyburz@slf.ch

Citation:

Kyburz, M. L., Sovilla, B., Gaume, J., & Ancey, C. (2020). Decoupling the role of inertia, friction, and cohesion in dense granular avalanche pressure build-up on obstacles. *Journal of Geophysical Research: Earth Surface*, 125, e2019JF005192. <https://doi.org/10.1029/2019JF005192>

Received 6 JUN 2019

Accepted 10 FEB 2020

Accepted article online 11 FEB 2020

Corrected 28 FEB 2020

This article was corrected on 28 FEB 2020. See the end of the full text for details.

Abstract Understanding the physical processes involved in snow avalanche-obstacle interaction is essential to be able to estimate the pressure exerted on structures. Although avalanche impact pressure has been measured in field experiments for decades, the underlying physical principles are still elusive. Previous studies suggest that pressure is increased due to the formation of an influenced flow region around the structure, the mobilized domain, which varies in size depending on snow properties such as snow cohesion. Here, we aim to better understand how cohesion, friction, velocity, and their interplay affect avalanche pressure buildup on structures. This is achieved by simulating the avalanche-obstacle interaction with a newly developed numerical model based on the discrete element method, using a cohesive bond contact law. The relevance of the model is tested by comparing simulated impact pressures with field measurements from the Vallée de la Sionne experimental site. Our results show that at the macroscale, impact pressure consists of the inertial, frictional, and cohesive contributions. The inertial and frictional contributions arise due to the existence, shape, and dimension of the mobilized domain. The cohesive contribution increases the particle contact forces inside the domain, leading up to a doubling of the pressure. Based on these physical processes, we propose a novel scaling law to reduce the problem of calculating the pressure induced by cohesive flows, to the calculation of cohesionless flows. These findings enhance our understanding of the interaction of cohesive granular flows, such as snow avalanches, and structures at the microscale and macroscale.

1. Introduction

How a flow behaves past an obstacle is a problem of fundamental importance in fluid mechanics. A related problem that has attracted considerable attention is the force exerted by the flow on an obstacle. For Newtonian fluids, two processes generate a force on an obstacle: the fluid pressure and the viscous forces. There is no general expression that holds for all flow configurations, but for some flows, analytical expressions have been derived. These concepts, however, can not always be extrapolated successfully for non-Newtonian fluids like snow avalanches (Ancey & Bain, 2015).

Indeed, snow avalanche pressure on obstacles is generally assessed by referring to two limiting cases. When the velocity is high, the impact pressure is calculated in a manner analogous to an inviscid fluid, where pressure is proportional to fluid density times the velocity squared ($p \propto \rho \cdot v^2$) (Baroudi & Thibert, 2009; Salm, 1966; Burkard et al., 1990; Sovilla et al., 2008a). If the velocity is low, snow avalanches are often approximated as cohesive granular flows (Bartelt & McArdell, 2009; Steinkogler et al., 2015) and are considered to be analogous to quasi-static granular flows, where impact pressure is proportional to gravity, density, and the immersion height of the obstacle in the medium ($p \propto \rho \cdot g \cdot h$) (Albert et al., 1999; Sovilla et al., 2010; Wieghardt, 1975).

Often the Froude number (equation (1)) is used to classify these two flow regimes. The case of fast avalanches is referred to as the inertial regime (supercritical, $Fr > 1$), and to the case of slow avalanches as the gravitational regime (subcritical, $Fr < 1$) (Mellor, 1968).

$$Fr = v / \sqrt{g \cdot h} \quad (1)$$

©2020. The Authors.

This is an open access article under the terms of the Creative Commons Attribution License, which permits use, distribution and reproduction in any medium, provided the original work is properly cited.

Table 1
Parameters for the DEM Simulations in the Gravitational and Inertial Regime

Parameter	Symbol	Unit	Gravitational plug flow	Inertial shear flow
Particle density	ρ_p	kg/m ³	500	500
Bulk density ^a	ρ_b	kg/m ³	370–430	300–366
Young's modulus	E	Pa	10 ⁵	10 ⁵
Cohesive strength	σ_{coh}	Pa	0.0–2.0 · 10 ⁴	0.0–2.0 · 10 ⁴
Friction coefficient	μ	—	0.5	0.5
Particle radius	r_p	mm	40 ± 8	40 ± 8
Depth-averaged velocity	v	m/s	2–8	15–40
Flow height	h	m	4.0	2.5

^aThe bulk density is not an input parameter but is mentioned here for illustrative reasons.

This is, however, a very coarse distinction as Köhler et al. (2018a) have recently shown that even for the same topography, the flow regimes can be manifold. It is assumed that snow properties, which are mechanically and thermodynamically very sensitive, are a main contributor to this diversity of flow behaviors as well as an important influence on avalanche-obstacle interaction behavior, which is not yet fully understood (Köhler et al., 2018b; Steinkogler et al., 2015). The problem of snow avalanche impact pressure has been investigated for some decades in field experiments (Gauer & Kristensen, 2016; Sovilla et al., 2008b; Thibert et al., 2015) and small-scale chute experiments (Hauksson et al., 2007; Moriguchi et al., 2009; Salm, 1964). Field measurements from snow avalanches (Sovilla et al., 2010, 2016) and studies on granular materials (Faug, 2015; Favier et al., 2013) indicate concurrently that the formation of force chains and cohesion, as well as the formation of a mobilized domain, where the flow is influenced by the presence of an obstacle, may increase the impact pressure of slow avalanches or granular flows in general. However, as Faug (2015) points out, further investigation on the size and shape of the mobilized domain, as well as the corresponding pressure on the obstacle, is needed to bridge the gap between processes at the microscale and the macroscopic force experienced by the obstacle.

The evidence that snow avalanches have a granular nature (Mellor, 1968; Salm, 1966) has prompted the idea to explore the interaction between avalanches and structures using the discrete element method (DEM). While multiple studies investigate the force exerted by a cohesionless granular material on an obstacle using DEM (Calvetti et al., 2017; Chanut et al., 2009; Teufelsbauer et al., 2011), only few have considered that of a cohesive material (e.g., Favier et al., 2013).

Hence, here we aim to identify which processes are involved in avalanche-obstacle interaction and assess how they contribute to pressure buildup on structures for a large range of Froude numbers and cohesion values. More specifically, we aim to clarify how cohesion influences the flow, the mobilized domain, and the impact pressure.

In this paper we tackle this issue by developing a new numerical model to reconstruct the processes occurring when an avalanche interacts with an obstacle using DEM with a cohesive bond contact model. We take advantage of the data acquired at the “Vallée de la Sionne” (VdIS) field site, in Valais, Switzerland (Ammann, 1999) to constrain the model parameters and test the model relevance. To compare simulated and measured impact pressures, we implement the geometry of a 20m high measurement pylon, where most of the measurements are taken and use two commonly observed avalanche scenarios. In VdIS, gravitational avalanches are often characterized by slowly moving snow (Table 1) forming a smooth basal layer which results in a flow with constant velocity over the whole flow height. The inertial regime is mostly typical of fast moving snow (Table 1), which often exhibits a vertical shear velocity profile due to the terrain roughness (Kern et al., 2009; Sovilla et al., 2008a).

By varying the cohesion and the velocity of the granular flow and analyzing the simulated impact pressure in each configuration, we identify different impact pressure contributions, especially the contribution of cohesion. In addition, we investigate the structure of the simulated flow around the obstacle at the particle level to identify the processes involved in the avalanche-obstacle interaction and to better interpret the measured and simulated pressures which arise at the obstacle. Finally, we back calculate the range of cohesion from

four gravitational snow avalanches measured at VdIS, to revisit the relevance of the cohesion values used in the simulations for real avalanches.

2. Materials and Methods

In this section we describe the newly developed DEM model we use to investigate the processes involved in avalanche-obstacle interaction. This model allows us to reproduce the flow of a granular medium, such as a snow avalanche, in the vicinity of the obstacle and to analyze the resulting impact pressure and flow behavior around the obstacle.

In the first part, we define the test case and present experimental data, which we use for the comparison with the simulations. The second part outlines how we model snow with DEM. In the third section, we present the model setup. The fourth section summarizes the most important parameters used in the simulations. Finally, we describe how we compare simulated impact pressures to field measurements. This paper's supporting information presents the details of the implementation of the numerical DEM, the contact model, as well as the model setup and procedure.

2.1. Experimental Data and Test Case

Over the past 20 years, a large set of field measurements has been collected at VdIS. Therefore, we choose the measurement data from this site as the test case to model avalanche flow and pressure in the present study. Among many other quantities, avalanche pressure and velocity are measured on a 20 m high pylon-like steel structure (Sovilla et al., 2010). The pylon is located on a flat slope beneath two couloirs, where avalanches releasing from a 1.5 km wide area converge (Ammann, 1999). Here, we use the term pressure to refer to the measured or simulated impact pressure on the obstacle, if not mentioned otherwise. At the pylon, the pressure is measured at the front of six cylinders distributed with 1 m vertical spacing (Sovilla et al., 2014). The velocity of the incoming flow is measured at the face of a wedge attached to the front of the pylon (Kern et al., 2010). These point measurements at the pylon are complemented by radar measurements, which provide information on the flow regime along the ~ 2.5 km long flow path (Köhler et al., 2018a).

Based on radar measurement data from VdIS, avalanche flows have been reclassified recently into seven categories (Köhler et al., 2018a). This highlights the complexity of avalanche flows, which also strongly depend on the specific terrain and the snow properties. In this study, however, we limit ourselves to two flow types, which are often observed at the VdIS test site, namely, the inertial shear flow and the gravitational plug flow regimes.

Field experiments have demonstrated, that in the inertial flow regime, which is mostly typical of fast and cold avalanches, the pressure is proportional to velocity squared. Throughout this paper, we refer to cold or warm avalanches as avalanches with prevailing snow temperatures below or above -1 °C, respectively. Previous research suggests that snow undergoes dramatic changes at this temperature, which consequently influences avalanche flow dynamics (Fischer et al., 2018; Köhler et al., 2018a; Steinkogler et al., 2015). The dense flows of inertial avalanches at VdIS rarely exceed a flow height of $h = 2.5$ m and often exhibit a sheared velocity profile (Kern et al., 2009). Typical velocities of the inertial dense flow at VdIS range from 10 m/s to 30 m/s (Sovilla et al., 2008a).

The gravitational regime is often observed for warm snow avalanches and features a linear pressure variation with flow depth. A typical gravitational plug flow avalanche flows at very low velocities up to a maximum of ~ 10 m/s, at the pylon location. At the VdIS test site these avalanches can build up maximum flow heights of 5–7 m and exert pressures in the range of 100–500 kPa (Sovilla et al., 2016). However, at VdIS, the peak flow heights are rarely maintained over longer time spans, but decrease with time. Heights of $h \lesssim 4$ m are more common for this kind of flow.

2.2. Modeling Snow using the Discrete Element Method

Our model is implemented within the framework of Itasca's commercial PFC software. This software implements the DEM method based on the soft-contact algorithm (Cundall & Strack, 1979) for interacting discrete particles.

Because of limited computational power, the number of snow crystals involved in large avalanches is prohibitive to be resolved as individual discrete elements in the model. Therefore, we consider the discrete particles to correspond to small snow agglomerates rather than individual ice crystals. Hence, the radius of

the particles in the simulations are normally distributed within the interval $32 \text{ mm} \leq r_p \leq 48 \text{ mm}$ corresponding to a mean value of $r_p = 40 \text{ mm}$. According to field surveys, this corresponds to an intermediate granule size (Bartelt & McArdell, 2009; Sovilla et al., 2008a; Steinkogler et al., 2015). Because snow particles are not resolved individually, the material properties of the discrete elements in the model must correspond to the macroscopic properties of the snow granules rather than the ice properties at the crystal level.

In DEM, the material's characteristics are not only influenced by the particles' properties. The dynamical behavior is primarily governed by the contact model, which comes into play whenever two particles interact with each other. A suitable contact law is therefore of prime importance to mimic the flowing snow in an avalanche. In the present work, a parallel bond contact model (Potyondy & Cundall, 2004) is used to model the mechanical behavior of snow. The model consists of two components: (1) a classical linear viscoelastic component consisting of a spring and a dashpot in the normal direction and a spring and a Coulomb friction limit in the tangential direction, as well as (2) an elastic-brittle cohesive bond in parallel to the linear component. The bond models the sintering and therefore cohesion of the real snow. Mechanically, it acts like a beam connecting the particles and can sustain normal and shear forces as well as bending and torsional loads. Similar to the sintering in snow, also in our simulations we allow for new bonds to form if a new contact occurs between two unbonded particles. Because the bond is in parallel to the linear component, the cohesionless behavior is conserved in any case, such as after bond breakage before a new bond forms.

2.3. Modeling the Interaction of the Avalanche Flow and Structures

In order to perform a systematic study of the influence of velocity and cohesion on impact pressure, we aim to impose the flow of the granular material independently from the particle and contact properties in the DEM model. Therefore, we propose a setup which enforces the flowing granular material (e.g., snow) to match a specific vertical velocity profile.

To achieve this, we isolate a finite volume of particles around the obstacle. The computational domain is 28 m high (z direction) and is confined with a wall at the bottom. This bottom wall mimics the gliding surface on which the avalanche flows. Transverse to the flow (y direction), the domain is 7 m wide and is limited by a periodic boundary condition. In the streamwise direction (x direction), the domain is 10 m long and is limited by boundary walls, segmented in height (Figures 1a and 1b). By moving the wall segments at different speeds at different heights, we can impose the velocity magnitude and profile to the particle volume. In this way the velocity past the obstacle can be controlled while also accounting for effects such as basal friction and shear dilatancy.

For the simulations, we use idealized plug and shear velocity profiles. In the gravitational plug flow, we impose a constant velocity over the whole flow height (Figure 1a). In the inertial shear flow, the velocity increases linearly from the bottom to the free surface of the granular flow (Figure 1b). Ranges for cohesion and velocity, velocity profiles, and flow heights are given in Table 1.

Gravity points in the negative z direction. While the average slope in the region of the VdIS pylon is approximately 20° , this approximation can be justified in the context of our test case because the terrain up to 10 m upstream of the pylon is nearly flat.

Figure 1c shows a vertical cross section through the obstacle implemented in the simulation, which is similar to the measurement pylon in VdIS. In the simulation the pressure and the velocity are sampled at the same temporal frequency as in VdIS. The simulated impact pressure and velocity at the obstacle are also sampled at the same locations as in VdIS. The locations are highlighted in Figure 1c in red and blue for the velocity and the pressure, respectively. The simulated impact pressure is determined by summing up the face-normal component of all contact forces acting on the measurement surface and dividing it by the sensor surface area.

With the exception of the comparison of simulations and measurements (sections 2.5 and 3.1), we always use the imposed velocity at the wall. To compare different simulations, we always use a representative value of contact force, velocity at the pylon, imposed velocity, confining pressure, and impact pressure, which corresponds to the value at midflow depth.

2.4. Model Parameters

While it is notoriously difficult to measure the mechanical properties of snow due to its heterogeneity (Gaume et al., 2015a; Gerling et al., 2017), even less is known about the mechanical properties of flowing snow in avalanches. As mentioned earlier, this applies particularly for cohesion, which is of central interest in the present study. Thus, most of the parameters and material properties applied in the simulations of this

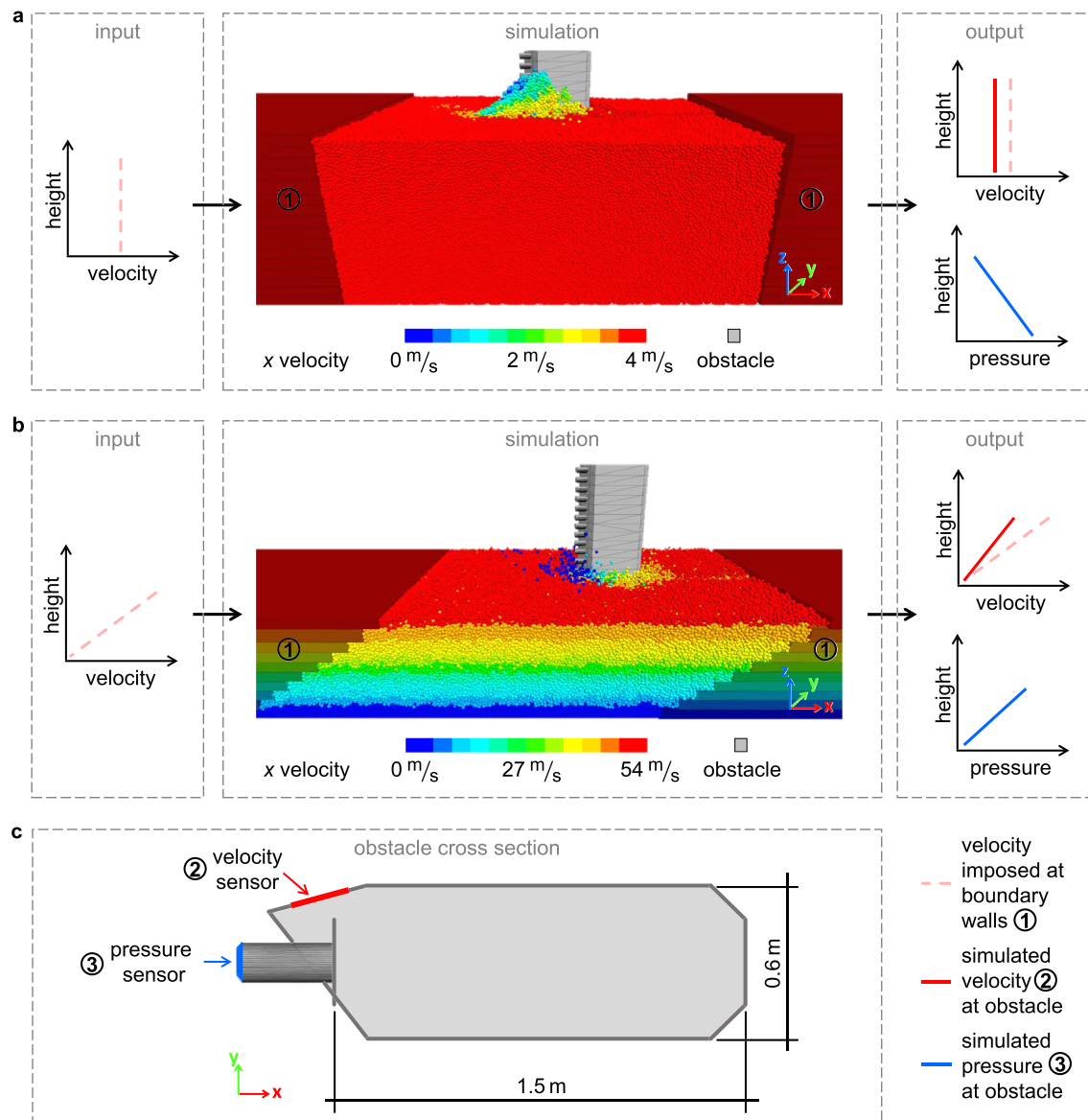


Figure 1. Panels (a) and (b) show the workflow for the DEM simulations of a plug flow and a shear flow velocity profile, respectively. The inputs of the simulations are on the left. The pictures in the middle show DEM simulations, where the boundary walls and the discrete elements are colored according to the velocity in the streamwise direction. The boundary walls and the static obstacle are shaded in gray. The outputs of the model are shown on the right. Panel (c) shows the cross section of the pylon with the location of the pressure and velocity sensors.

study are estimated rather than rigorously measured or calibrated with values within typical ranges as used and suggested by other authors for snow.

As mentioned in section 2.1, gravitational and inertial avalanches have different snow and flow properties. In the present article we want to focus on the influence of velocity and cohesion on the impact pressure. Hence, in our parametric study we only vary the cohesion as well as the flow height and the velocity according to the two flow regimes given in Table 1. Parameters such as the friction coefficient $\mu = 0.5$ (Gaume et al., 2015b, 2018; Steinkogler et al., 2015), Young's modulus E , particle radius r_p (section 2.2), and particle density $\rho_p = 500 \text{ kg/m}^3$ of a single discrete element are constant in all simulations. In contrast to ρ_p , the bulk density ρ_b is the volumetric average density including voids between particles in a spherical control volume with a radius of $5.0 \cdot r_p$. Hence, ρ_b varies as a result of cohesion and shear rates, ranging from 370 to 430 kg/m^3 in the gravitational plug flows and from 300 to 365 kg/m^3 in the inertial shear flows. The ranges of these bulk densities agree well with the values from field and experimental studies (Bartelt & McArdell, 2009; Platzer et al., 2007; Steinkogler et al., 2015).

For the particles' Young's modulus, we use a value of $E = 10^5$ Pa in all simulations, which is in the lower range of the values used by Gaume et al. (2015b) for modeling snow slabs and in the range of reported values from the literature (Gerling et al., 2017; Scapozza, 2004; Shapiro et al., 1997). For Young's modulus of the cohesive bond, we use the same value as for the particles. The cohesive strength of the bond is set to $\sigma_{\text{coh. less}} = 0$ Pa for cohesionless simulations and varied between $0 \text{ kPa} < \sigma_{\text{coh}} \leq 20 \text{ kPa}$ otherwise. The upper limit corresponds roughly to the values reported by Shapiro et al. (1997) for snow with densities from 320 to 420 kg/m^3 and is the same range as that used by Gaume et al. (2015b). In the present study we use the local Bond number (equation (2)) instead of σ_{coh} to analyze the influence of the cohesive strength.

$$Bo = \sigma_{\text{coh}}/p_{\text{conf}} \quad (2)$$

This dimensionless number is the rescaled cohesion, defined as the cohesive strength divided by the confining pressure p_{conf} (Roy et al., 2017), where the confining pressure is the vertical component of the local stress tensor $p_{\text{conf}} \equiv \sigma_{zz}$.

The parameters discussed here are summarized in Table 1.

2.5. Comparing Simulated Impact Pressure Profiles to Field Measurements

In this section we describe how we compare the simulated impact pressure and field measurements to test the DEM model's capacity to reproduce impact pressure measurements in a selected flow scenario. To reproduce a flow scenario, we impose a velocity profile at the boundary walls in the simulation, as depicted in Figures 1a and 1b. The resulting velocity profile at the pylon is directly dependent on the imposed one, but is slightly altered due to the presence of the obstacle influencing the flow.

On the condition that the simulated and the measured velocity profile at the pylon are similar, we can compare the resulting impact pressure profiles for this scenario. Hence, we use the velocity profile at the pylon as a boundary condition by matching the simulated and measured velocity profile. We therefore impose an idealized plug or shear velocity profile (section 2.3) such that the resulting velocity at the pylon closely matches the measured velocity. The only free parameter is the cohesion, which to date cannot be measured in experiments and can only be estimated for the simulations (section 2.4). The other parameters in the simulations are kept constant as described in Table 1.

3. Results

The following section presents the results of our study on the influence of velocity and cohesion on the avalanche pressure on the VdIS pylon. The results are divided into four parts. In the first step, we compare the simulated impact pressure to field measurements of snow avalanches from VdIS to test whether the model proposed in section 2 is able to reproduce field measurements. Second, we show the results of the parametric study, where we vary velocity and cohesion in our simulation. There we analyze how impact pressure is influenced by changes in these two variables. In the third step, we analyze the flow around the obstacle at the microscale to better interpret and understand the influence of velocity and cohesion on the impact pressure. In the fourth step, we analyze the range of cohesion, the pressures, and pressure fluctuations in gravitational avalanches with regard to the results from the previous sections.

3.1. Comparison of DEM Simulations With Field Measurements

For the comparison of simulations with measurements, we select examples of field measurements of a gravitational plug flow and an inertial shear flow from the VdIS archive, respectively.

In the case of the gravitational flow, we select measurements performed in a warm avalanche (archive number 20103003 in the VdIS database), which was released naturally on 30 December 2009. From these measurements we extract a short time sequence in the order of 0.5 s to obtain the pressure and velocity profile. In Figure 2a these measurements are compared to a simulation with an imposed plug velocity profile of 10 m/s, a flow height of 4 m, resulting in the red velocity profile of ~ 8 m/s at the pylon (Figure 2a, left panel). For the cohesive strength we choose a value of $\sigma_{\text{coh}} = 15.6$ kPa which is high considering the range of σ_{coh} given in Table 1, as expected from a typical warm plug flow avalanche.

The qualitative trend of the simulated pressure profile agrees with the measured pressure profile, which increases linearly with the flow depth (Figure 2a, right panel). However, the simulated pressure increases

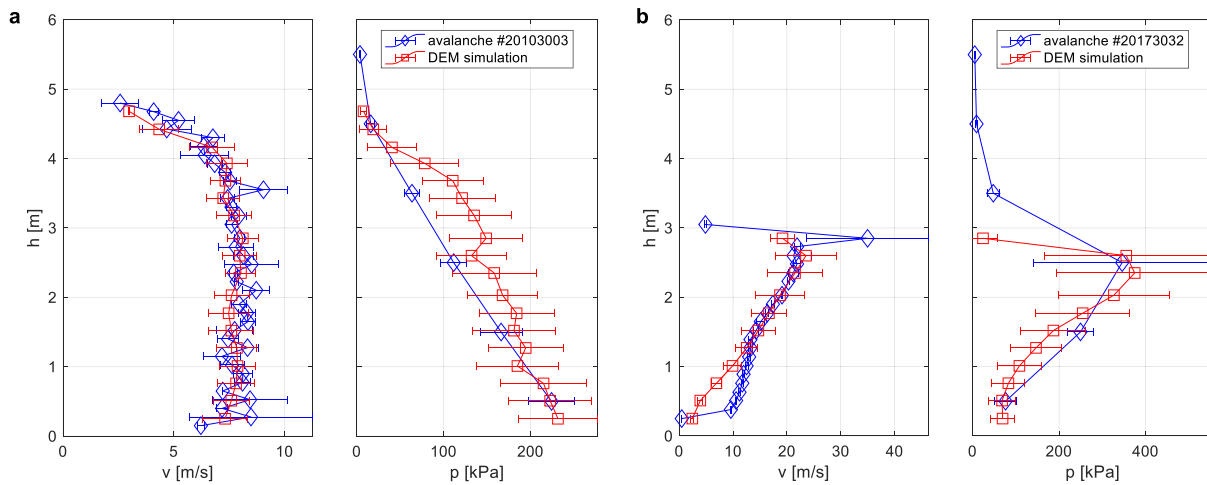


Figure 2. Panels (a) and (b) show the comparison of simulated (red squares) and measured (blue diamonds) velocity and pressure profiles for an example of a plug flow and a shear flow, respectively. The error bars indicate the standard deviation from the mean value of the pressure or velocity. The interpolating lines between the data points are only a visual aid.

at a slightly higher rate near the free surface of the flow and at a slightly lower rate below ~ 3.5 m than in the real-scale experiment.

In the case of the inertial shear flow we choose the measurement of avalanche # 20173032, which was released artificially on 8 March 2017. In Figure 2b this measurement is compared to a simulation with a flow height of 2.5 m and an imposed shear velocity profile of 0–20 m/s, resulting in the red velocity profile at the pylon shown in Figure 2b, left panel. Due to the idealization of the shear velocity profile as a linear profile, the simulated velocity profile shows small deviations with the measurements in the lower layers of the flow, at a flow height of ~ 1.0 m. For this scenario we choose a cohesive strength of $\sigma_{\text{coh}} = 1.25$ kPa. As it would be expected for an inertial shear flow, the selected cohesion is considerably lower than that of the gravitational plug flow. The small mismatch between the measured and simulated velocity profiles does not seem to affect the pressure profiles in Figure 2b, right panel. The two impact pressure profiles show a very good agreement.

In order to test the relevance of our model in simulating the correct pressure for a larger range of velocities and cohesions, we vary the cohesive strength and velocity in our simulations according to the ranges given in Table 1.

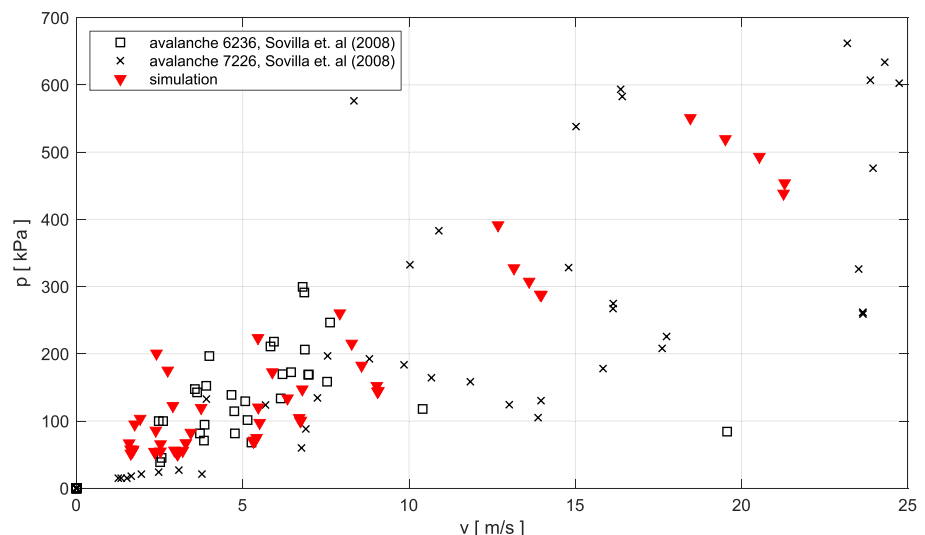


Figure 3. Comparison of simulated (red triangles) and measured (black symbols) impact pressure versus velocity.

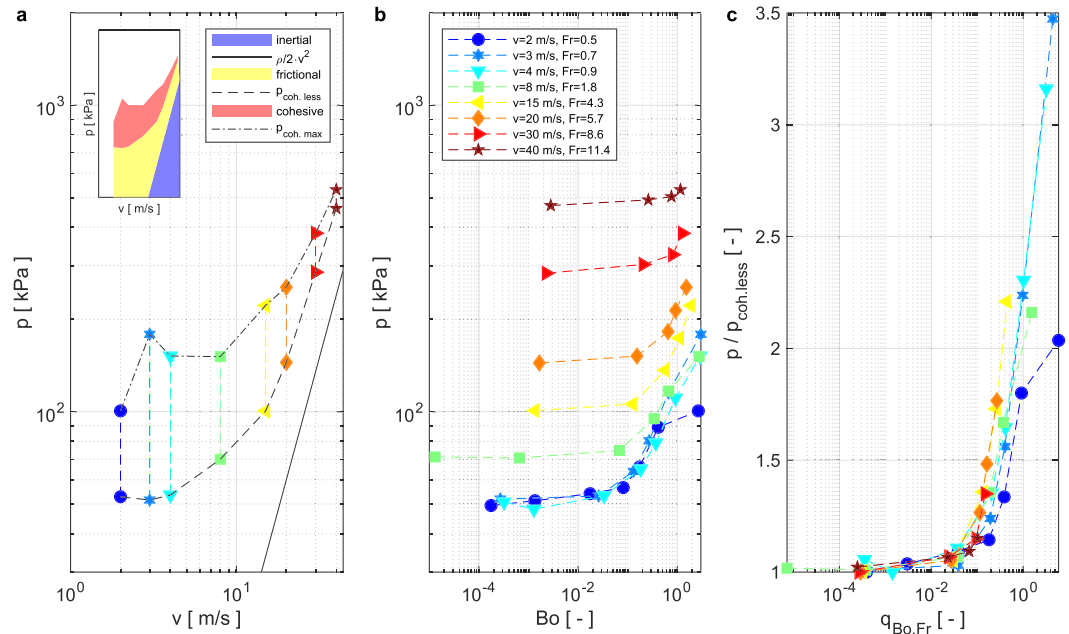


Figure 4. Panel (a) shows the simulated pressure as a function of velocity with an illustration of the inertial (blue), frictional (yellow), and cohesive (red) pressure contributions in the inset. Panel (b) shows the simulated pressure for different Fr (colors) as a function of the Bond number. Panel (c) shows the pressure normalized by the corresponding cohesionless pressure plotted against the Bond to Froude number ratio $q_{Bo,Fr}$. In panels (b) and (c) the dashed interpolating lines between the data points are only a visual aid.

In Figure 3, we compare the simulated impact pressures to field measurements of two avalanches (# 7226 and # 6236, published by Sovilla et al., 2008a). We can see that the simulated and measured impact pressure values in Figure 3 show good agreement over a wide range of avalanche velocities. For low velocities up to 10 m/s, the scatter of the simulated data is in the same range as the scatter of the measured data. The large scatter of the measurements for velocities higher than 10 m/s is very likely to be caused by the variability of the snow properties in the avalanches (Köhler et al., 2018b). The scatter in the simulations is smaller because many snow properties are kept constant (Table 1). Specifically, the scatter of the simulated impact pressure is caused only by the variation of cohesion, flow height, or imposed velocity.

3.2. Influence of Velocity and Cohesion on Impact Pressure

In this section we analyze the influence of velocity and cohesion on impact pressure. For this purpose, we vary both quantities systematically in the ranges given in Table 1.

Figure 4a shows the simulated impact pressures p on the obstacle plotted over a range of velocities. Here we plot the impact pressure of cohesionless simulations connected by the dashed black line, and the simulations with the strongest cohesion $\sigma_{coh} = 20$ kPa connected by the dash-dotted black line. We observe that the dashed and the dash-dotted line only vary little at slow velocities under 4 m/s, as found earlier for cohesionless granular materials (Albert et al., 1999; Wieghardt, 1975). For velocities higher than 8 m/s, the pressure increases gradually, for the cohesive and the cohesionless case.

In this plot we identify three pressure contributions at the macroscale. The contributions are separated by the black lines in Figure 4a, and visualized by the colored areas in the inset.

We define the first impact pressure contribution as the inertial contribution, which is proportional to velocity squared $p \propto v^2 \cdot \rho/2$ (Salm, 1966), similarly to the hydrodynamic impact pressure of inviscid fluids. This contribution is visualized in Figure 4a by the blue area in the inset and the black solid line, which is calculated using a constant density $\rho = 300$ kg/m³ as suggested by Burkard et al. (1990). In the log-log plot in Figure 4a the slope of the cohesionless pressure curve (dashed line) reaches a maximum of 1.9 between 30 and 40 m/s, very close to the theoretical value 2.0 given by the v^2 proportionality (solid line). Hence, Figure 4a shows that $p \propto v^2 \cdot \rho/2$ is only a good approximation for the pressure of fast flows in the inertial regime ($v \gtrsim 20$ m/s).

For flows where $v \leq 15$ m/s, we observe that the lowest simulated pressures, which are connected by the dashed black line and correspond to cohesionless simulations, are well above the solid black line. Hence, we define the second contribution as the pressure difference between the dashed and the solid black line at a constant velocity and refer to it as the frictional pressure contribution. It is highlighted with the yellow area in the inset. The frictional contribution arises due to the granular nature of the flow which we inherently simulate with DEM, in contrast to the flow of an inviscid fluid. The pressure increase due to this contribution is $\sim 30\%$ (50 kPa) of the maximum pressure for $v < 8$ m/s and decreases monotonically for $v > 8$ m/s. Hence, the frictional contribution is mostly relevant for gravitational flows ($2 \leq v \leq 8$ m/s).

The third pressure contribution is the cohesive contribution, visualized with the red area in the inset. We define it as the pressure difference between the dash-dotted and the dashed black line at a constant velocity. Thus, the cohesive contribution is the difference between impact pressure of a cohesive and a cohesionless simulation. While frictional processes between particles might still occur in the red area, they are less relevant with increasing cohesion because the cohesive bonds inhibit the relative movement between the particles. Hence, the increase in impact pressure is caused by the presence of cohesion in the granular material. From Figure 4a we find that, for the maximum cohesion $\sigma_{\text{coh}} = 20$ kPa, the maximum pressure increase due to cohesion is 70% (127 kPa) at 3 m/s and 14% (70 kPa) at 40 m/s, respectively. Hence, similarly to the frictional contribution also the cohesive contribution is more relevant for gravitational flows than for inertial flows.

Figure 4b shows the pressure plotted against the Bond number Bo to investigate the influence of cohesive strength on impact pressure. For all Fr values, we observe that at small Bo (equation (2)), pressure is a very weak function of Bo . In contrast, we find that for large Bo values the pressure is affected significantly by cohesion (Bo). For increasing velocity, and thus Froude number, the pressure curves are gradually shifted toward higher Bond numbers.

In order to obtain a more universal description of the pressure curves, we compensate for this shift by introducing a new dimensionless number, which is the ratio of the Bond and the Froude number $q_{Bo,Fr} = Bo/Fr$. In Figure 4c, we normalize the absolute pressure p by the impact pressure of the cohesionless flow $p_{\text{coh. less}}$ at the same speed and plot it against $q_{Bo,Fr}$. By normalizing the pressure in this way, we consider only the pressure increase, which is caused by the presence of cohesion. As Figure 4c demonstrates, the pressure data collapse almost onto a single curve for the suggested choice of normalization. The curves show that the pressure is amplified by cohesion predominantly for the flows with low velocities. The largest amplifications are observed at 3 and 4 m/s, where the pressure of the cohesive flow is up to 3.5 and 3.2 times higher, respectively, than the pressure of the cohesionless flow.

3.3. Analysis of the Mobilized Domain and Origin of the Pressure Amplification at the Microscale

In order to understand the origin of the pressure amplifications, we analyze the flow around the pylon at the particle level (microscale) and compare selected simulations. First, we give a general overview of three scenarios with different velocities and cohesions. In the following sections 3.3.1 and 3.3.2, we analyze the influence of velocity (Fr) and cohesion (Bo) separately.

We define the mobilized domain as the volume in the flow, where the contact forces between particles adjacent to the obstacle coherently exceed a threshold. With respect to contact forces, we consider only the force component normal to the contact plane. We define this threshold as the median of the contact forces in a control volume around the pylon. In the present analysis, the median of the contact forces is more representative of the undisturbed force level than the mean value because the mean is increased by very high force values in the mobilized domain.

Figure 5 shows the comparison of the mobilized domain for three sample simulations. The first and second rows show simulations of gravitational flows ($Fr = 0.9$) with no and strong cohesion, respectively. The third row shows the simulation of an inertial flow ($Fr = 11.4$) with strong cohesion.

In Figures 5a, 5d, and 5g we find that force chains stronger than average are only observed in the same region where the velocity of particles is reduced due to the presence of the obstacle. Indeed, the mobilized domains in the velocity field and the contact forces agree well in terms of size and shape. For the two gravitational examples (first and second rows), the mobilized domain has an almost circular shape and is located upstream of the obstacle. Qualitatively, the contact forces in the mobilized domain away from the pylon increase from top to bottom in both Figures 5b and 5e. This increase is even more pronounced in the mobilized domain in

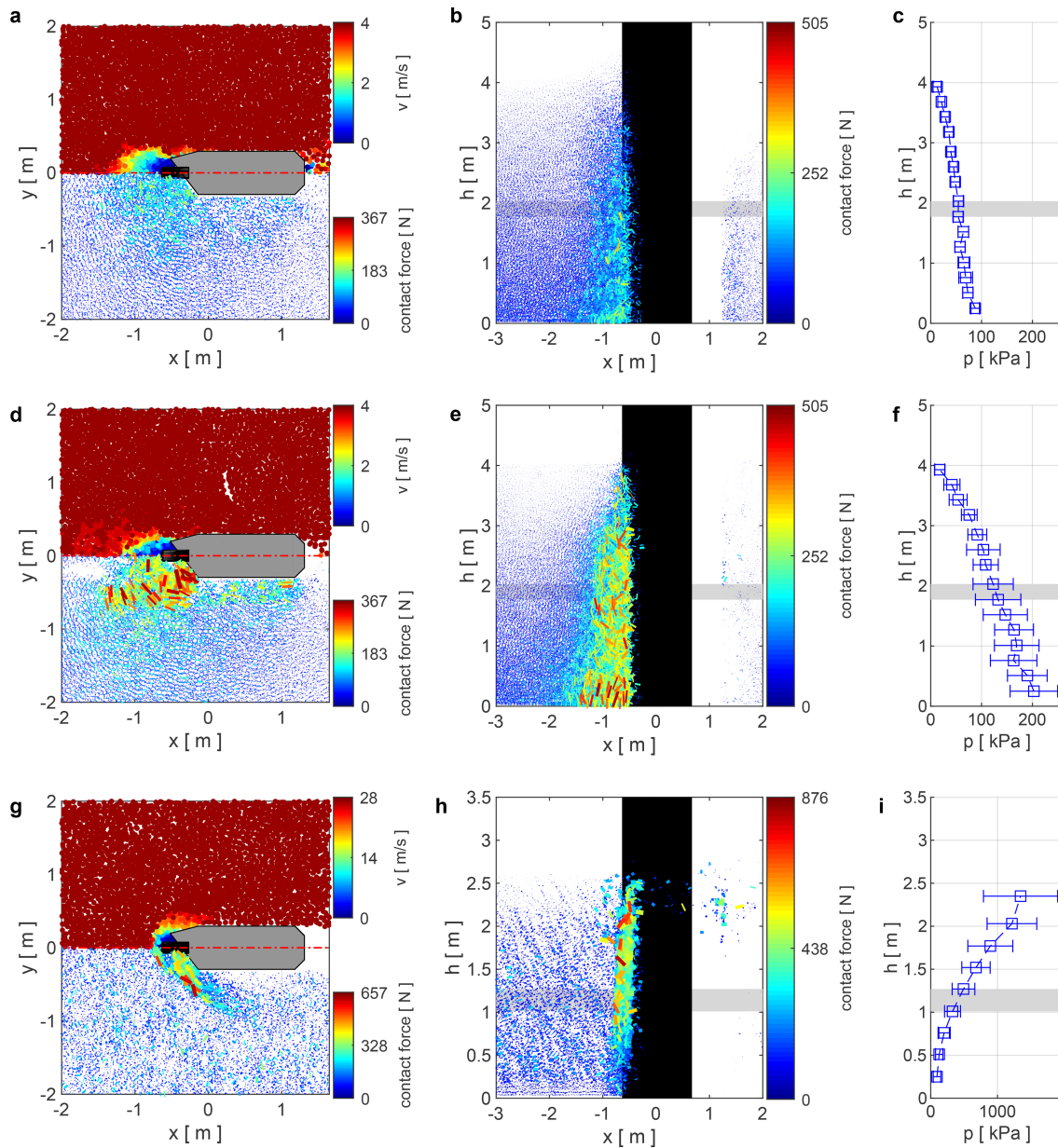


Figure 5. Analysis of the flow and contact forces around the pylon at the microscale. Panels (a)–(c) show a gravitational flow ($Fr = 0.9$) with no cohesion ($\sigma_{coh} = 0.0$ kPa). Panels (d)–(f) show a gravitational flow ($Fr = 0.9$) with high cohesion ($\sigma_{coh} = 10.0$ kPa). Panels (g)–(i) show an example of an inertial flow ($Fr = 11.4$) with high cohesion ($\sigma_{coh} = 10.0$ kPa). Panels (a), (d), and (g) show a horizontal section view through the flow in the middle of the flow height as indicated by the gray area in the other panels. The upper half in panels (a), (d), and (g) shows the velocity distribution. The lower half shows interparticle contact forces whose strength is visualized through the line thickness and color. Panels (b), (e), and (h) show the vertical section view in the x - z plane located in the middle of the pylon (red dash-dotted line in panels (a), (d), and (g)). The extent of the pylon is visualized by the black area. Panels (c), (f), and (i) show the impact pressure profiles with the standard deviation of the temporal pressure fluctuations from its mean value indicated by the error bars.

the vicinity of the obstacle. Not only do the contact forces increase with increasing depth below the surface of the dense flow, but the mobilized domain also grows larger in size. In the simulation with strong cohesion (panel d, $\sigma_{coh} = 10.0$ kPa), the mobilized domain is considerably larger and contact forces are stronger than in the cohesionless case (panel a, $\sigma_{coh} = 0.0$ kPa).

In the inertial flow (panel g, $\sigma_{coh} = 10.0$ kPa), we observe very strong contact forces only in the vicinity of the obstacle. The shape of the mobilized domain is similar to a bow-wave at the leading edge of the pylon.

When comparing the pressure profiles in Figures 5c and 5f to the Figures 5b and 5e, we observe higher pressure at the bottom or for high cohesion, where the mobilized domain and contact forces are larger. Aside

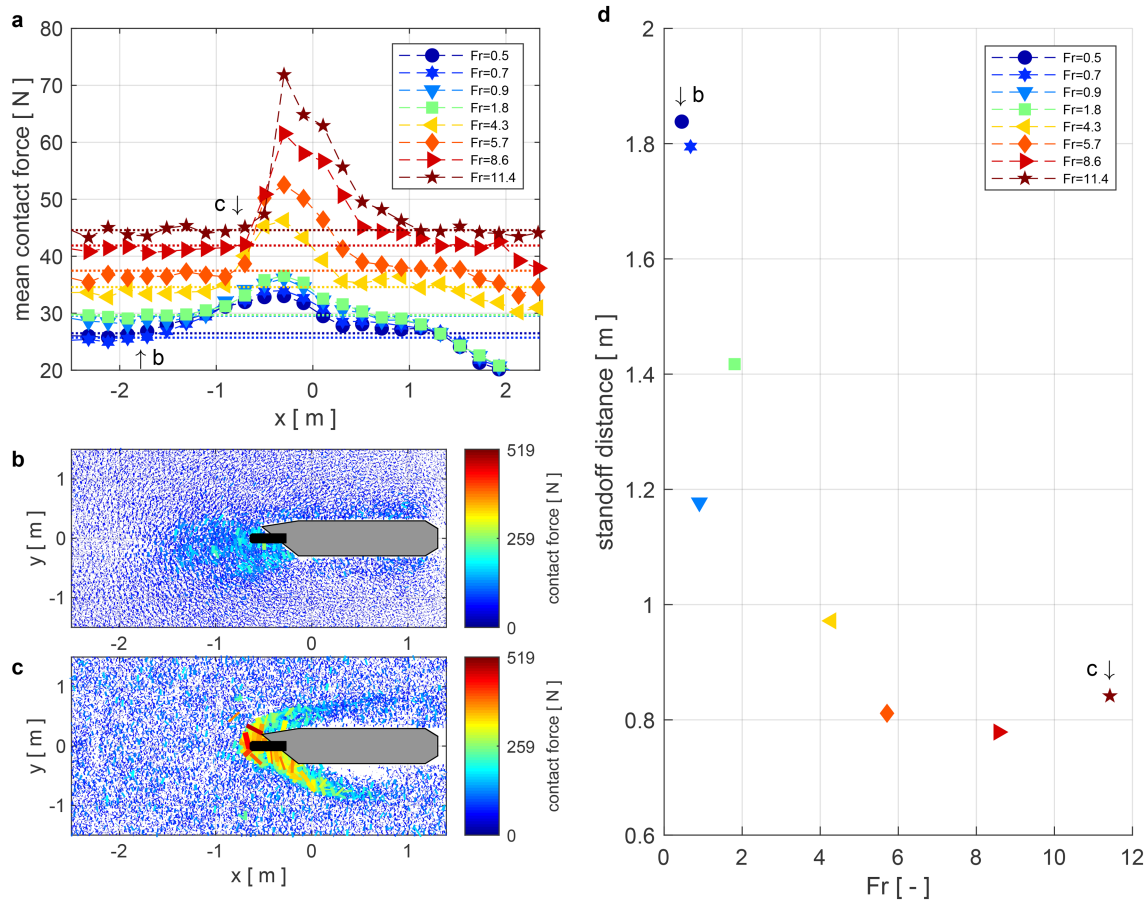


Figure 6. Influence of the Froude number on the mobilized domain and the standoff distance. Panel (a) shows the mean contact force upstream of the obstacle in streamwise direction for different Froude numbers and $Bo = 0.0$. The dotted lines correspond to the median contact force in simulations with the same color. Panels (b) and (c) show horizontal section views at midheight from the simulation with the lowest and the highest Froude number from panel (a), respectively. The lines indicate the force chains whose strength is visualized through the line thickness and color. Panel (d) shows the standoff distances of the mobilized domain as a function of Fr for cohesionless flows.

from the increase in the pressure itself, pressure fluctuations also increase in the flow with high cohesion. In contrast, for the inertial flow regime (Figures 5h and 5i), the strongest contact forces and pressures are located at the top where the flow velocity is the highest.

3.3.1. Influence of the Froude Number on the Mobilized Domain and Impact Pressure

In Figure 5, we show that the geometry of the mobilized domain varies in different scenarios. Here we want to examine how the shape changes when varying Froude numbers. To exclude the influence of cohesion we only consider cohesionless simulations.

Figure 6a shows the mean contact forces as a function of distance from the obstacle (position 0) and for different Fr (colored symbols). Each point in the plot represents the local contact force averaged in volumes across the whole domain width at varying streamwise positions (x direction). The dotted lines in Figure 6a indicate the median of the contact forces in the whole domain, which is used as the threshold for the mobilized domain as defined earlier.

Figure 6a shows that the shape and location of the mobilized domain change as a function of the Froude number. This is visualized in Figures 6b and 6c, which display the contact forces for the simulations corresponding to the Froude numbers $Fr = 0.5$ and $Fr = 11.4$, respectively. Similarly to Figure 5, we find a circle-shaped mobilized domain for the lowest Froude number $Fr = 0.5$ (Figure 6b). Figure 6c reveals that the mobilized domain is pushed downstream if the Froude number is increased. In this case strong contact forces concentrate just upstream of the obstacle. This leads to the sharp increase in the mean contact force in Figure 6a for high Fr compared to low Fr .

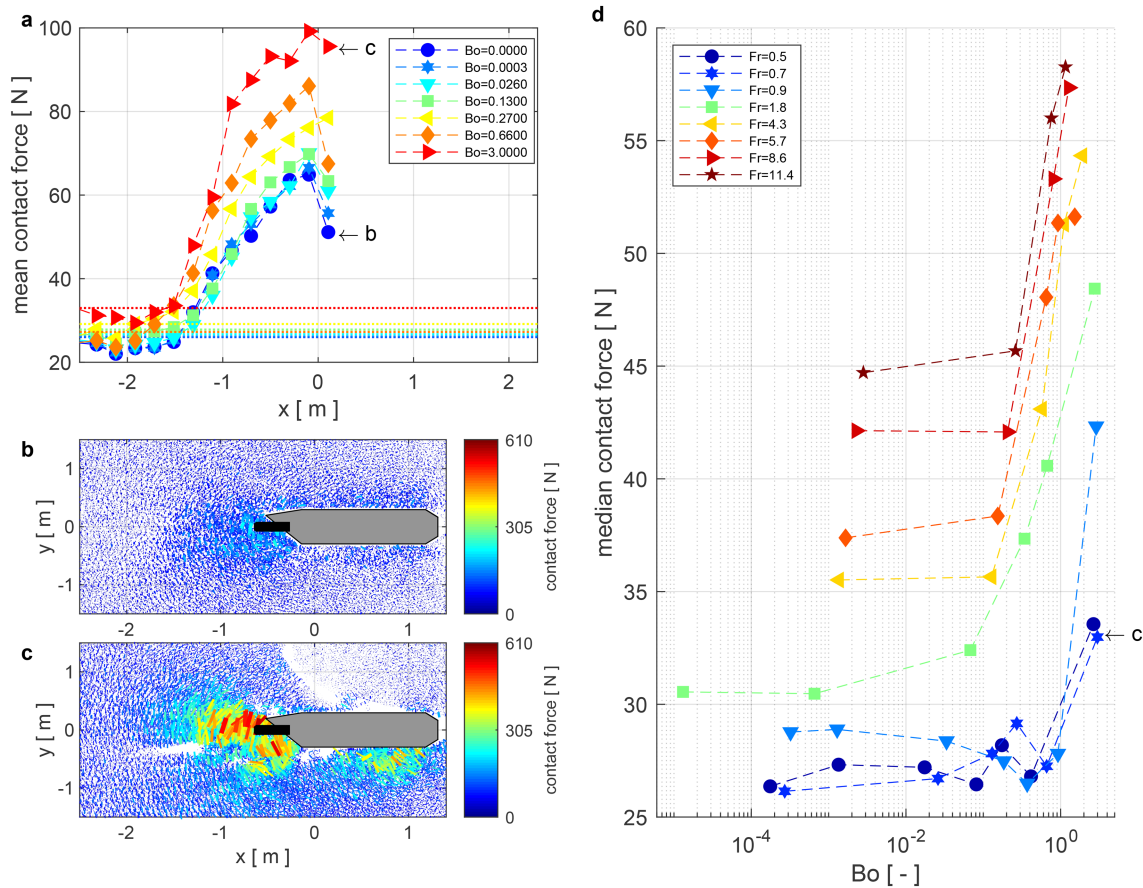


Figure 7. Influence of cohesion on contact forces and the mobilized domain. Panel (a) shows the mean contact force upstream of the obstacle in streamwise direction for different Bond numbers (different colors and symbols) at $Fr = 0.7$. The dotted lines correspond to the median contact force in simulations with the same color. Panels (b) and (c) show horizontal section views at midheight from the cohesionless case and the most cohesive simulation from panel (a), respectively. The lines indicate the force chains whose strength is visualized through the line thickness and color. Panel (d) shows the median contact force as a function of Bo , and for different Fr (colors and symbols).

To quantify the size of the mobilized domain in a single number, we use the standoff distance. Similarly to Faug (2015), we define it as the furthest point in the mobilized domain upstream of the obstacle's leading edge. Hence, the standoff distance defined here depends on the choice of the threshold which is used to distinguish between the free flow and the mobilized domain. However, even for a different threshold, the definition of the mobilized domain with the median force proves to be very robust, and the standoff distance alters only marginally. Here, we use the standoff distance to compare the size of the mobilized domains across all cohesionless simulations. Figure 6d shows that the standoff distance decreases dramatically from 1.84 to ~ 1.0 m with increasing Froude numbers in the range of $0 \leq Fr \leq 5$. For $Fr > 5$, the values of the standoff distance level out at around 0.8 m.

3.3.2. Influence of the Bond Number on the Mobilized Domain and Impact Pressure

In this section we investigate the influence of cohesion on the mobilized domain and the pressure on the obstacle. Similarly to the analysis in the previous section 3.3.1, we consider contact forces to be an indicator of the disturbance of the structure on the flow. However, here we only take contacts directly upstream of the structure into account, because these are considered the most relevant for pressure buildup. If a larger region in the y direction is considered, higher forces in the mobilized domain are averaged out and are therefore less evident. Figure 7a shows the mean contact forces as a function of streamwise location for Bond numbers varying between $Bo = 0.0$ and $Bo = 3.0$. In Figure 7a, the flow has a Froude number of $Fr = 0.7$. Again we consider the median of the contact forces as an indicator of the overall force level (dotted lines in Figure 7a).

In contrast to Figure 6a all curves in Figure 7a have a similar shape. In addition, the standoff distance is almost constant around 1.5 m for all cases, and the dotted lines show that contact forces are enhanced by increasing cohesion. This is even more pronounced for local forces in the mobilized domain just upstream

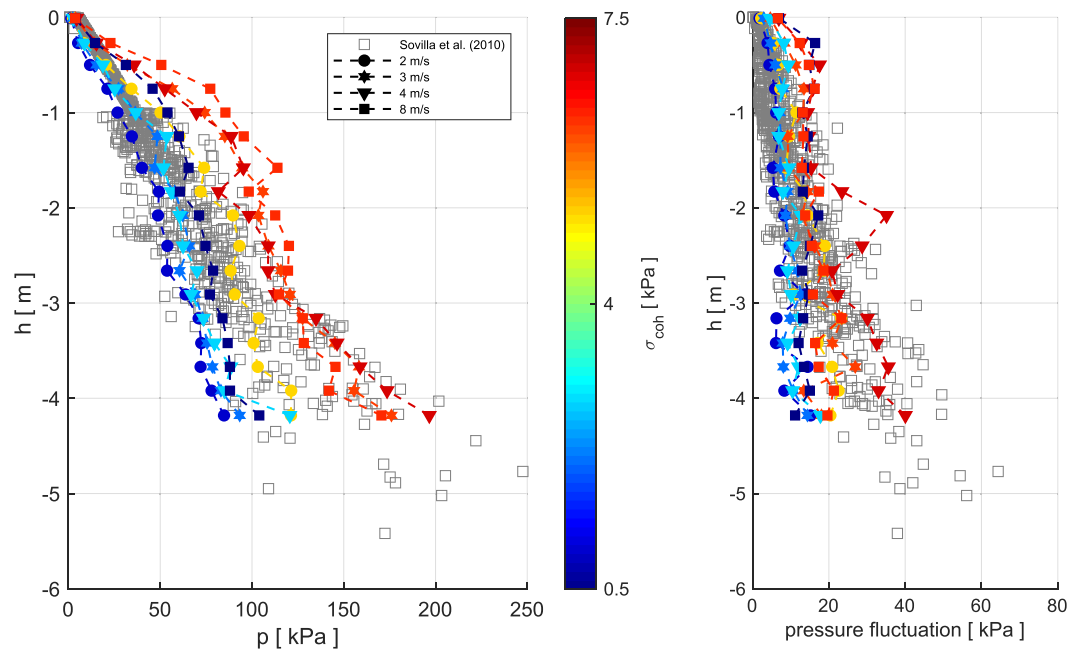


Figure 8. Panel (a) shows the simulated (colored symbols) and measured (gray squares, from Sovilla et al., 2010) pressure of gravitational avalanches on the VdS pylon. Panel (b) shows the pressure fluctuations alone for the same avalanche and simulation data as in panel (a).

from the obstacle. There, the peak contact forces differ considerably more between low and strong cohesion than the median contact force. For the example of $Fr = 0.7$ given in Figure 7a, the peak force (highest red triangle) is ~ 3 times higher than the median of the contact forces (red dotted line) for the highly cohesive case. In the cohesionless simulation, the peak value (highest dark blue circle) is only 2.5 times higher than the median contact force (dark blue dotted line). A sectional view of the flow around the pylon in the middle of the flow height illustrates this for the case with no cohesion (panel b, $Bo = 0.0$) and strong cohesion (panel c, $Bo = 3.0$). In these two pictures it is obvious that very strong cohesion heavily intensifies contact forces in the vicinity of the obstacle, while the shape and size of the mobilized domain remain largely unchanged. In panel (c), the cohesion is so high that the granular material fails along clearly visible fracture lines.

In Figure 7d, we compare the median contact force of all simulations with varying velocity and cohesion, and plot this as a function of the respective Bond number. Here we find that similarly to the pressure in Figure 4b, the median contact forces also increase with increasing Fr . Moreover, the median contact forces also exhibit a weak dependency on Bo for low Bo values and a strong dependency for large Bo values.

3.4. Pressure and Range of Cohesion in Gravitational Avalanches

As mentioned in section 2.4, we vary cohesion in simulations in the range of 0.0–20.0 kPa. From Figures 4c and 7d we learn that pressure is only amplified by cohesion if a critical threshold of the Bond-to-Froude ratio is exceeded. By comparing simulated to measured pressures of gravitational avalanches, we aim to evaluate which range of cohesive strengths in our simulations can be used to reproduce the pressure values observed in reality. In Figure 8, we show the measurement data of three gravitational avalanches published by Sovilla et al. (2010) represented by the gray squares. In these measured warm dense avalanches, velocity ranges from 1 to 8 m/s. The simulated pressure is colored according to the cohesive strength and has different markers for varying velocity. The temporal pressure fluctuations are illustrated by the error bars in panel (a) and are separately plotted as a function of the flow height in Figure 8b for all simulations of panel (a).

We find in Figure 8a that cohesive strengths in the range of 0.5–7.5 kPa fit the measurement data well for the velocity range 2–8 m/s. The different symbols indicating velocity in Figure 8a show that avalanche speed has very little influence on the pressure. In contrast, it is apparent from the colors that flows with less cohesion exert lower pressures than flows with elevated cohesion.

Already in Figure 5, we observed that pressure fluctuations are larger in flows with higher cohesion. This trend is clearly confirmed by Figure 8b. Similar to the measured fluctuations, fluctuations in the simulations

also increase with increasing flow depth as well. Although Figure 8b shows good overall agreement between measurements and simulations, the simulated fluctuations are greater than those from measurements at the flow free surface and increase less deeper within the avalanche. Similarly to the pressure itself, fluctuations are smaller and larger in simulations with little and high cohesion, respectively.

4. Discussion

4.1. Modeling Avalanche-Obstacle Interaction With DEM

In section 2, we describe our newly developed DEM model to study the interaction between avalanches and structures. By comparing simulated pressure profiles and pressure profile from field measurements, we show that by treating avalanches as granular flows and applying the DEM, the numerical model is able to reproduce flow-depth and velocity squared proportional pressure profiles as well as temporal pressure fluctuations. Furthermore, the simulated pressure values are in the same order as measured values over a wide range of avalanche velocity (Figure 3). Particularly at velocities lower than 5 m/s the simulated impact pressure values agree well with measurements from avalanches # 6236 and # 7226. Only at higher velocities we observe a significant difference between the scattering of the simulated and measured impact pressure. This is probably because we only vary few parameters (Table 1) in our parametric study.

Further limitations of the presented model become apparent due to the differences in pressures and pressure fluctuations between simulations and measurements (Figures 2a, 2b, and 8). First, the current parallel-bond contact model does not allow for plastic compaction of the granular material. We assume that compaction influences not only pressure at the bottom of the avalanche flow, due to the weight of the snow above, but also across the whole flow height where the snow impacts the obstacle (Gauer & Jóhannesson, 2009). Second, variation in the radii of particles is small, whereas in natural avalanches, particles are typically larger at the surface of the flow due to particle segregation, which may affect the pressure distribution (Kern, 2000). To obtain a broad understanding of the influence of cohesion in various avalanche scenarios we choose a large range of cohesion ($0.0 \text{ kPa} \leq \sigma_{\text{coh}} \leq 20.0 \text{ kPa}$) values and apply it to the whole range of velocities (Table 1). We put these cohesive values into perspective by back calculating the cohesion range from four avalanche measurements. From the calculations and comparisons in section 3.1 and 3.4, the measurements of these slow avalanches are found to correspond to cohesion values of $0.5 \text{ kPa} \leq \sigma_{\text{coh}} \leq 15.6 \text{ kPa}$ in the simulations. Although the back-calculated cohesion values agree well with values of tensile strength of snow reported by other authors (Jamieson & Johnston, 1990; Mellor, 1974; Shapiro et al., 1997; Yamanoi & Endo, 2002), they are probably only valid for the same choice of the other parameters stated in Table 1.

In this study, we used mechanical snow properties from the literature, which are mostly derived from studies on the mechanics of undisturbed snow. In contrast, avalanche snow may undergo large deformations and transitions (Steinkogler et al., 2015; Valero et al., 2015). Therefore, the stated values must be considered with care in the context of this study. Hence, in the future it would be important to collect data on the mechanical properties of snow granules from avalanches.

The qualitative trend of all results shown in this study have, however, proven to be very robust to changes in any of these parameters. For example, if ρ_p is increased, the absolute pressure value increases as well, but pressure proportionality with flow depth and velocity squared and the trends shown in section 3.3.1, 3.3.2, 3.2–3.4 remain qualitatively the same. Given this qualitative robustness of the results to changes in the particle properties and because we use a standard cohesive contact model as well as a generic model setup, we believe that the physical understanding gained in this study may also be relevant for similar processes, where cohesive granular flows interact with rigid structures.

4.2. Impact Pressure Contributions at the Macroscale

In the inset of Figure 4a, we visualize and highlight the inertial, frictional, and cohesive impact pressure contributions. The complex interplay between these contributions in avalanche dynamics are investigated for the first time in this study. It is important to note that all three contributions are present for the whole range of Fr , but with changing importance as a share of the entire impact pressure.

The inertial contribution is known from other fields (e.g., fluid dynamics, granular flows) and is proportional to density and velocity squared. This v^2 proportionality is confirmed by the slope of the dashed black line in Figure 4a, which is ~ 2 for high velocities ($v \gtrsim 20 \text{ m/s}$). Hence, we confirm that avalanche pressure is governed primarily by inertial impact for Froude numbers close to or greater than 10 (Faug, 2015;

Thibert et al., 2008; Voellmy, 1955). The frictional contribution is most pronounced at low Fr and arises due to the granular nature of the flow. It is, therefore, also present in cohesionless granular flows (Albert et al., 2001; Chehata et al., 2003). Thus, even a hypothetical cohesionless avalanche would exert considerably higher pressures on an obstacle at low Fr , compared to the inertial contribution alone.

The cohesive contribution is also highest at low Fr and constitutes up to 70% of the entire impact pressure for the range of cohesion from Table 1. If we consider the range of back-calculated cohesion ($0.5 \text{ kPa} \leq \sigma_{\text{coh}} \leq 15.6 \text{ kPa}$) the largest pressure amplification factor due to cohesion is 2.1 with respect to the cohesionless case. Furthermore, we show that cohesion is only relevant for a pressure increase above a certain threshold, where the slopes of the curves in Figure 4b increase dramatically. The idea of a critical cohesion threshold is also supported by other studies (Favier et al., 2013; Steinkogler et al., 2015). Most likely, below this threshold the flow behaves similarly to a cohesionless flow as long as collisional forces are strong enough to break the cohesive bonds between particles. If the cohesive strength is above this threshold value, the bonds cannot be broken anymore by the collisional forces. Thus, the flow exhibits a cohesive behavior (section 3.3.2) and impact pressure is amplified.

Because the cohesion threshold is included in the range of the back-calculated cohesion values we assume that real avalanches are most likely subject to this transition between cohesive and nearly cohesionless flow behavior. Similarly to the sharp transition of granulation behavior at the threshold temperature -1°C reported by Steinkogler et al. (2015), we demonstrate that also here small changes in cohesion around the cohesion threshold, above which pressure is amplified, may lead to substantial changes in pressure.

We also observe that the cohesion threshold varies with Fr and assume that this is due to the competing effect of cohesive and inertial forces in the snow. We take this into account by defining the Bond to Froude ratio $q_{\text{Bo},Fr}$. Moreover, we decouple the cohesive pressure contribution from the frictional and inertial contribution by normalizing the impact pressure of a cohesive flow with the cohesionless pressure. The collapse of the data from Figure 4b onto a single curve in Figure 4c shows that we find a scaling for the impact pressure of a cohesive granular as a function of the cohesionless pressure as well as Bo and Fr . This scaling allows us to estimate the impact pressure of a cohesive granular flow by calculating the pressure of cohesionless flow and multiplying by the factor given in the curve in Figure 4c. This is expedient because the problem of cohesionless granular flow impacting an obstacle has been studied in the past (e.g., Albert et al., 2001).

4.3. Microscale Processes of Impact Pressure Buildup

In this study, we confirm the existence of the mobilized domain postulated by Faug (2015), even in cohesionless granular flows. Hence, the mobilized domain owes its presence to the granular nature and the force chains in the granular flow, rather than the presence of cohesion. Consequently, the mobilized domain in cohesionless flows is most likely the origin of the frictional pressure contribution (yellow area in inset of Figure 4a).

Our results show that the shape of the mobilized domain can be described using the Froude number only. For low Fr , the domain has an approximately circular shape and is located mainly upstream of the obstacle (Figure 6b). If the Froude number is increased, the mobilized domain is “pushed” gradually downstream by the flow. For the highest Froude numbers, the mobilized domain has the shape of a bow wave (Figure 6c).

Here, we use the standoff distance (section 3.3.1) to characterize the extent of the mobilized domain. Figure 6d shows that for increasing Fr , the standoff distance decreases dramatically from a maximum of ~ 2.0 m in the range of $Fr < 5$, and then levels out at around 1 m for $Fr > 5$. This result agrees qualitatively with the findings of Cui and Gray (2013) and Faug et al. (2002) on the standoff distance of granular bow shocks and size of mobilized domains, respectively. Interestingly, a similar dependency is found experimentally between the drag coefficient of a wall and Fr in a mud flow by Tiberghien et al. (2007), as well as for the hydrodynamic impact pressure of debris flows and Fr by Proske et al. (2011). Quantitatively, however, the maximum standoff distance in all simulations is considerably smaller than the 3.5–7.0 m estimated by Sovilla et al. (2016) using the theory of Faug (2015) for the same structure. Furthermore, it is important to bear in mind that the size of the mobilized domain and therefore the standoff distance probably differs substantially for other geometries.

We also show that cohesion neither influences the size nor shape of the mobilized domain, but changes the level of the contact forces inside the domain. As a general rule, we observe that the median contact forces

increase with increasing cohesion. Our results confirm the observations of Favier et al. (2013), who found that cohesion increase leads to a densification of the contact network and to an increase in the temporal contact persistency. Figure 7d shows that the dependency of the median contact force and cohesion is not linear. Indeed, the median of the contact forces are almost constant for low Bond numbers but increase sharply if a particular Bo is exceeded. The resemblance of Figure 4b to Figure 7d clearly indicates that the pressure increase due to cohesion at the macroscale is directly linked to the intensified contact forces at the microscale. While further proof is needed, we assume that the frictional and cohesive contributions observed at the macroscale can be linked to processes at the particle scale. The frictional contribution arises due to frictional and collisional processes between particles, which causes the mobilized domain to form around a structure due to jamming or building of force chains. Thereby, the force of the incoming flow probably acts on the larger apparent surface of the obstacle, which is the outline of the mobilized domain, and it is transmitted and concentrated at the obstacle surface through the force chains. By increasing the cohesion between particles, the force transmission from the apparent surface to the obstacle is enhanced and results in higher pressure on the obstacle surface.

5. Conclusions

In this study we present a newly developed DEM model to investigate the interaction between dense snow avalanches and obstacles. We show that the model is able to reproduce the pressure profiles and the range of temporal pressure fluctuations exerted by avalanches on the VdIS pylon for a wide range of Froude numbers and cohesion values. This indicates that approximating avalanches as granular flows and applying DEM allows us to capture the most important physical processes involved in avalanche-obstacle interaction.

We also identify, however, some limitations of the model. First, the contact model does not allow for compaction of snow, and particle segregation cannot occur because the particles are not flowing freely. Second, particle properties are estimated from values found in the literature, which are based on the mechanical behavior of undisturbed snow samples. Hence, to obtain relevant results in future investigations on the mechanical properties and contact behavior of snow avalanche granules will be needed.

In our study we identify three pressure contributions, which are of varying importance depending on avalanche speed. The inertial contribution, which is proportional to velocity squared and density, is most important at high avalanche velocities. The frictional contribution arises due to the granular nature of the flow and is therefore inherently present in cohesionless flows. Hence, depending on the granulometry, the impact pressure of slow avalanches is increased by this frictional contribution even without the presence of cohesion, such as in cold avalanches. In agreement with previous studies, we find growing evidence that the formation of force chains and the existence of a mobilized domain around the structure in cohesionless flows are factors leading to elevated pressures at low Fr compared to the impact pressure in Newtonian fluids (Faug, 2015; Favier et al., 2013; Sovilla et al., 2010). The shape of this mobilized domain smoothly changes from a nearly circular shape upstream of the obstacle for low Fr , into a bow-wave-like shape for high Fr .

The cohesive contribution increases the impact pressure of a cohesionless flow by a maximum factor of 2.1 if a critical cohesion value is exceeded, such as in warm avalanches. We find that this increase of impact pressure is caused by the amplification of contact forces within the entire cohesive flow, but especially within the boundaries of the mobilized domain. Surprisingly, the shape and size of the domain are barely influenced by cohesion as assumed in other studies (Faug, 2015; Rognon et al., 2008).

Furthermore, we find a scaling relating the pressure of cohesive and cohesionless flows. This allows us to reduce the problem of calculating the pressure of a cohesive granular flow, to calculating the pressure of a cohesionless flow, which has been investigated in the past (Albert et al., 2001; Albaba et al., 2015; Calvetti et al., 2017; Chanut et al., 2009; Moriguchi et al., 2009).

Thanks to the identification of the three pressure contributions at the macroscale and the underlying processes at the particle level, this study contributes to our understanding of the buildup of impact pressure of cohesive granular flows on narrow structures. Finally, as we use a standard cohesive bond contact model and the qualitative results are not affected by changes of the properties of the granular material, we are convinced that this study may be relevant not only for snow avalanches but also for the interaction of structures and flows of cohesive granular materials in general.

Acknowledgments

Michael Kyburz, Betty Sovilla, and Christophe Ancey acknowledge the Swiss National Science Foundation for funding this project “Pressure on obstacles induced by granular snow avalanches” (Grant 200021_169640). Johan Gaume acknowledges financial support from the Swiss National Science Foundation (Grant PCEFP2_181227). The supporting information and the code to be used with the Itasca PFC3D software to reproduce the data presented in this paper are available in the open access data repository Zenodo, which is financed by the Horizon 2020 project OpenAIRE and hosted by CERN. The associated entry can be accessed via Kyburz M. L., Sovilla, B., Gaume J., and Ancey C. (2019). Decoupling the role of inertia, friction, and cohesion in dense granular avalanche pressure buildup on obstacles [Supporting Information]. Zenodo (<https://doi.org/10.5281/zenodo.3239031>). We would like to thank the Editor Ton Hoitink, the Associate Editor Michele Bolla Pittaluga, as well as Thierry Faug and two anonymous reviewers for their helpful comments.

References

Albaba, A., Lambert, S., Nicot, F., & Chareyre, B. (2015). Relation between microstructure and loading applied by a granular flow to a rigid wall using DEM modeling. *Granular Matter*, 17(5), 603–616. <https://doi.org/10.1007/s10035-015-0579-8>

Albert, R., Pfeifer, M., Barabasi, A.-L., & Schiffer, P. (1999). Slow drag in a granular medium. *Physical Review Letters*, 82, 205–208. <https://doi.org/10.1103/PhysRevLett.82.205>

Albert, I., Sample, J. G., Morss, A. J., Rajagopalan, S., Barabási, A.-L., & Schiffer, P. (2001). Granular drag on a discrete object: Shape effects on jamming. *Physical Review E*, 64(061), 303. <https://doi.org/10.1103/PhysRevE.64.061303>

Ammann, W. J. (1999). A new Swiss test-site for avalanche experiments in the Vallée de la Sionne/Valais. *Cold Regions Science and Technology*, 30(1), 3–11. [https://doi.org/10.1016/S0165-232X\(99\)00010-5](https://doi.org/10.1016/S0165-232X(99)00010-5)

Ancey, C., & Bain, V. (2015). Dynamics of glide avalanches and snow gliding. *Reviews of Geophysics*, 53, 745–784. <https://doi.org/10.1002/2015RG000491>

Baroudi, D., & Thibert, E. (2009). An instrumented structure to measure avalanche impact pressure: Error analysis from Monte Carlo simulations. *Cold Regions Science and Technology*, 59(2), 242–250. <https://doi.org/10.1016/j.coldregions.2009.05.010>

Bartelt, P., & McArdell, B. W. (2009). Granulometric investigations of snow avalanches. *Journal of Glaciology*, 55(193), 829–833. <https://doi.org/10.3189/002214309790152384>

Burkard, A., Gubler, H. U., & Salm, B. W. (1990). Berechnung von Fließlawinen: eine Anleitung für Praktiker mit Beispielen. Mitteilungen des Eidgenössischen Instituts für Schnee- und Lawinenforschung vol. 47, Eidgenössisches Institut für Schnee- und Lawinenforschung, Davos.

Calvetti, F., di Prisco, C. G., & Vairaktaris, E. (2017). DEM assessment of impact forces of dry granular masses on rigid barriers. *Acta Geotechnica*, 12(1), 129–144. <https://doi.org/10.1007/s11440-016-0434-z>

Chanut, B., Faug, T., & Naaim, M. (2009). Mean force on a wall overflowed by dense granular avalanches: Discrete numerical simulations. *AIP Conference Proceedings*, 1145(1), 609–612. <https://doi.org/10.1063/1.3180000>

Chehata, D., Zenit, R., & Wassgren, C. R. (2003). Dense granular flow around an immersed cylinder. *Physical Fluids*, 15(6), 1622–1631. <https://doi.org/10.1063/1.1571826>

Cui, X., & Gray, J. M. N. T. (2013). Gravity-driven granular free-surface flow around a circular cylinder. *Journal of Fluid Mechanics*, 720, 314–337. <https://doi.org/10.1017/jfm.2013.42>

Cundall, P. A., & Strack, O. D. L. (1979). A discrete numerical model for granular assemblies. *Géotechnique*, 29(1), 47–65. <https://doi.org/10.1680/geot.1979.29.1.47>

Faug, T. (2015). Macroscopic force experienced by extended objects in granular flows over a very broad Froude-number range. *The European Physical Journal E*, 38(5), 34. <https://doi.org/10.1140/epje/i2015-15034-3>

Faug, T., Lachamp, P., & Naaim, M. (2002). Experimental investigation on steady granular flows interacting with an obstacle down an inclined channel: Study of the dead zone upstream from the obstacle. Application to interaction between dense snow avalanches and defence structures. *Natural Hazards and Earth System Science*, 2(3/4), 187–191. <https://doi.org/10.5194/nhess-2-187-2002>

Favier, L., Daudon, D., & Donzé, F.-V. (2013). Rigid obstacle impacted by a supercritical cohesive granular flow using a 3D discrete element model. *Cold Regions Science and Technology*, 85, 232–241. <https://doi.org/10.1016/j.coldregions.2012.09.010>

Fischer, J.-T., Kaitna, R., Heil, K., & Reiweger, I. (2018). The heat of the flow: Thermal equilibrium in gravitational mass flows. *Geophysical Research Letters*, 45, 11,219–11,226. <https://doi.org/10.1029/2018GL079585>

Gauer, P., & Jóhannesson, T. (2009). The design of avalanche protection dams: Recent practical and theoretical developments. chap. Loads on walls, pp. 77–94, Climate Change and Environmental Risks, EUROPEAN COMMISSION.

Gauer, P., & Kristensen, K. (2016). Four decades of observations from NGI’s full-scale avalanche test site Ryggfonn—Summary of experimental results. *Cold Regions Science and Technology*, 125, 162–176. <https://doi.org/10.1016/j.coldregions.2016.02.009>

Gaume, J., Chambon, G., Eckert, N., Naaim, M., & Schweizer, J. (2015a). Influence of weak layer heterogeneity and slab properties on slab tensile failure propensity and avalanche release area. *Cryosphere*, 9(2), 795–804. <https://doi.org/10.5194/tc-9-795-2015>

Gaume, J., Gast, T., Teran, J., van Herwijnen, A., & Jiang, C. (2018). Dynamic anticrack propagation in snow. *Nature communications*, 9(1), 3047. <https://doi.org/10.1038/s41467-018-05181-w>

Gaume, J., van Herwijnen, A., Chambon, G., Birkeland, K. W., & Schweizer, J. (2015b). Modeling of crack propagation in weak snowpack layers using the discrete element method. *Cryosphere*, 9(5), 1915–1932. <https://doi.org/10.5194/tc-9-1915-2015>

Gerling, B., Löwe, H., & van Herwijnen, A. (2017). Measuring the elastic modulus of snow. *Geophysical Research Letters*, 44, 11,088–11,096. <https://doi.org/10.1002/2017GL075110>

Hauksson, S., Pagliardi, M., Barbolini, M., & Jóhannesson, T. (2007). Laboratory measurements of impact forces of supercritical granular flow against mast-like obstacles. *Cold Regions Science and Technology*, 49(1), 54–63. <https://doi.org/10.1016/j.coldregions.2007.01.007>

Jamieson, J., & Johnston, C. (1990). In-situ tensile tests of snow-pack layers. *Journal of Glaciology*, 36(122), 102–106. <https://doi.org/10.3189/S002214300000561X>

Kern, M. (2000). *Inverse grading in granular flow*, pp. 336 Pp. Lausanne: EPFL.

Kern, M. A., Bartelt, P. A., & Sovilla, B. (2010). Velocity profile inversion in dense avalanche flow. *Annals of Glaciology*, 51(54), 27–31. <https://doi.org/10.3189/172756410791386643>

Kern, M., Bartelt, P., Sovilla, B., & Buser, O. (2009). Measured shear rates in large dry and wet snow avalanches. *Journal of Glaciology*, 55(190), 327–338. <https://doi.org/10.3189/002214309788608714>

Köhler, A., Fischer, J.-T., Scandroglia, R., Bavay, M., McElwaine, J., & Sovilla, B. (2018b). Cold-to-warm flow regime transition in snow avalanches. *Cryosphere*, 12, 3759–3774. <https://doi.org/10.5194/tc-12-3759-2018>

Köhler, A., McElwaine, J., & Sovilla, B. (2018a). GEODAR data and the flow regimes of snow avalanches. *Journal of Geophysical Research: Earth Surface*, 123, 1272–1294. <https://doi.org/10.1002/2017JF004375>

Mellor, M. (1968). Avalanches (*Crrrel Research Reports*): Army Dept/US/.

Mellor, M. (1974). *A review of basic snow mechanics*: US Army Cold Regions Research and Engineering Laboratory.

Moriguchi, S., Borja, R. I., Yashima, A., & Sawada, K. (2009). Estimating the impact force generated by granular flow on a rigid obstruction. *Acta Geotechnica*, 4(1), 57–71. <https://doi.org/10.1007/s11440-009-0084-5>

Platzler, K., Bartelt, P., & Kern, M. (2007). Measurements of dense snow avalanche basal shear to normal stress ratios (S/N). *Geophysical Research Letters*, 34, L07501. <https://doi.org/10.1029/2006GL028670>

Potyondy, D., & Cundall, P. (2004). A bonded-particle model for rock. *International Journal of Rock Mechanics and Mining Sciences*, 41(8), 1329–1364. <https://doi.org/10.1016/j.ijrmmms.2004.09.011>

Proske, D., Suda, J., & Hübl, J. (2011). Debris flow impact estimation for breakers. *Georisk: Assessment and Management of Risk for Engineered Systems and Geohazards*, 5(2), 143–155. <https://doi.org/10.1080/17499518.2010.516227>

- Rognon, P. G., Roux, J.-N., Naaïm, M., & Chevoir, F. (2008). Dense flows of cohesive granular materials. *Journal of Fluid Mechanics*, 596, 21–47. <https://doi.org/10.1017/S0022112007009329>
- Roy, S., Luding, S., & Weinhart, T. (2017). A general(ized) local rheology for wet granular materials. *New Journal of Physics*, 19(4), 043014. <https://doi.org/10.1088/1367-2630/aa6141>
- Salm, B. (1964). Anlage zur untersuchung dynamischer wirkungen von bewegtem schnee. *Zeitschrift für angewandte Mathematik und Physik ZAMP*, 15(4), 357–375. <https://doi.org/10.1007/BF01601287>
- Salm, B. (1966). Contribution to avalanche dynamics. *Scientific Aspects of Snow and Ice Avalanche*, 69, 199–214.
- Scapozza, C. (2004). *Entwicklung Eines Dichte-Und Temperaturabhängigen Stoffgesetzes Zur Beschreibung Des Visko-Elastischen Verhaltens Von 2Chnee*. ETH Zürich: Phdthesis. <https://doi.org/10.3929/ethz-a-004680249>
- Shapiro, L. H., Johnson, J., Sturm, M., & Blaisdell, G. (1997). Snow mechanics: Review of the state of knowledge and applications. *CRREL Report*, 97-3, 40.
- Sovilla, B., Faug, T., Köhler, A., Baroudi, D., Fischer, J.-T., & Thibert, E. (2016). Gravitational wet avalanche pressure on pylon-like structures. *Cold Regions Science and Technology*, 126, 66–75. <https://doi.org/10.1016/j.coldregions.2016.03.002>
- Sovilla, B., Kern, M., & Schaer, M. (2010). Slow drag in wet-snow avalanche flow. *Journal of Glaciology*, 56(198), 587–592. <https://doi.org/10.3189/002214310793146287>
- Sovilla, B., Margreth, S., Schaer, M., & Ancey, C. (2014). Taking into account wet avalanche load for the design of pylon-like structures. In *Proceedings of International Snow Science - Montana State University Library*, pp. 727–732.
- Sovilla, B., Schaer, M., Kern, M., & Bartelt, P. (2008a). Impact pressures and flow regimes in dense snow avalanches observed at the Vallée de la Sionne test site. *Journal of Geophysical Research*, 113, F01010. <https://doi.org/10.1029/2006JF000688>
- Sovilla, B., Schaer, M., & Rammer, L. (2008b). Measurements and analysis of full-scale avalanche impact pressure at the Vallée de la Sionne test site. *Cold Regions Science and Technology*, 51(2), 122–137. <https://doi.org/10.1016/j.coldregions.2007.05.006>
- Steinkogler, W., Gaume, J., Löwe, H., Sovilla, B., & Lehning, M. (2015). Granulation of snow: From tumbler experiments to discrete element simulations. *Journal of Geophysical Research: Earth Surface*, 120, 1107–1126. <https://doi.org/10.1002/2014JF003294>
- Teufelsbauer, H., Wang, Y., Pudasaini, S. P., Borja, R. I., & Wu, W. (2011). DEM simulation of impact force exerted by granular flow on rigid structures. *Acta Geotechnica*, 6(3), 119. <https://doi.org/10.1007/s11440-011-0140-9>
- Thibert, E., Baroudi, D., Limam, A., & Berthet-Rambaud, P. (2008). Avalanche impact pressure on an instrumented structure. *Cold Regions Science and Technology*, 54(3), 206–215. <https://doi.org/10.1016/j.coldregions.2008.01.005>
- Thibert, E., Bellot, H., Ravanat, X., Ousset, F., Pulfer, G., Naaïm, M., et al. (2015). The full-scale avalanche test-site at Lautaret Pass (French Alps). *Cold Regions Science and Technology*, 115, 30–41. <https://doi.org/10.1016/j.coldregions.2015.03.005>
- Tiberghien, D., Laigle, D., Naaïm, M., Thibert, E., & Ousset, F. (2007). Experimental investigations of interaction between mudflow and an obstacle. *Debris-flow hazards mitigation: mechanics, prediction, and assessment*, pp. 281–292.
- Valero, C. V., Jones, K. W., Bühler, Y., & Bartelt, P. (2015). Release temperature, snow-cover entrainment and the thermal flow regime of snow avalanches. *Journal of Glaciology*, 61(225), 173–184. <https://doi.org/10.3189/2015JG14J117>
- Voellmy, A. (1955). Über die Zerstörungskraft von Lawinen (On the destructive forces of avalanches). *Schweizerische Bauzeitung*, 73, 159–162. <https://doi.org/10.5169/seals-61891>
- Wiegardt, K. (1975). Experiments in granular flow. *Annual Review of Fluid Mechanics*, 7(1), 89–114. <https://doi.org/10.1146/annurev.fl.07.010175.000513>
- Yamanoi, K., & Endo, Y. (2002). Dependence of shear strength of snow cover on density and water content. *Seppyo*, 64(4), 443–451. <https://doi.org/10.5331/seppyo.64.443>

References From the Supporting Information

- Christoffersen, J., Mehrabadi, M., & Nemat-Nasser, S. (1981). A micromechanical description of granular material behavior. *Journal of Applied Mechanics*, 48(2), 339–344. <https://doi.org/10.1115/1.3157619>
- Crandall, S. H., Lardner, T. J., Archer, R. R., Cook, N. H., & Dahl, N. C. (1978). *An introduction to the mechanics of solids* (second ed.). Singapore: McGraw-Hill.
- Itasca Consulting Group, Inc (2014). *Particle flow code in 3D, Version 5.0 software documentation*. Minneapolis: Itasca Consulting Group Inc.

Erratum

The originally published version of Figure 4a was replaced after publication; during changes in revision, an error was introduced in the code used to produce Figure 4a, which has since been corrected. The correction led to a parallel shift of one straight line in Figure 4a, which did not affect the results of the study. This may be considered the authoritative version of record.